

Fast and realistic large-scale structure from machine-learning-augmented random field simulations

Davide Piras^{1*}, Benjamin Joachimi¹, and Francisco Villaescusa-Navarro^{2,3}

¹*Department of Physics and Astronomy, University College London, Gower Street, London, WC1E 6BT, UK*

²*Center for Computational Astrophysics, Flatiron Institute, 162 5th Avenue, New York, NY, USA 10010*

³*Department of Astrophysical Sciences, Princeton University, 4 Ivy Lane, Princeton, NJ 08544 USA*

Accepted XXX. Received YYY; in original form ZZZ

ABSTRACT

Producing thousands of simulations of the dark matter distribution in the Universe with increasing precision is a challenging but critical task to facilitate the exploitation of current and forthcoming cosmological surveys. Many inexpensive substitutes to full N -body simulations have been proposed, even though they often fail to reproduce the statistics of the smaller, non-linear scales. Among these alternatives, a common approximation is represented by the lognormal distribution, which comes with its own limitations as well, while being extremely fast to compute even for high-resolution density fields. **In this work, we train a machine learning model to transform projected lognormal dark matter density fields to more realistic dark matter maps, as obtained from full N -body simulations.** We detail the procedure that we follow to generate highly correlated pairs of lognormal and simulated maps, which we use as our training data, exploiting the information of the Fourier phases. We demonstrate the performance of our model comparing various statistical tests with different field resolutions, redshifts and cosmological parameters, proving its robustness and explaining its current limitations. The augmented lognormal random fields reproduce the power spectrum up to wavenumbers of $1\ h\ \text{Mpc}^{-1}$, the bispectrum and the peak counts within 10%, and always within the error bars, of the fiducial target simulations. Finally, we describe how we plan to integrate our proposed model with existing tools to yield more accurate spherical random fields for weak lensing analysis, going beyond the lognormal approximation.

Key words: large-scale structure of Universe – dark matter – software: simulations – methods: statistical

1 INTRODUCTION

The best current model to describe our Universe is the Λ CDM model, which prescribes the existence of a cosmological constant Λ associated with dark energy, together with cold dark matter (CDM) and ordinary matter (baryons; see e.g. Dodelson 2003). In particular, the Λ CDM model predicts that dark matter is about five times more abundant than ordinary matter, with galaxies forming along the cosmic web structure woven by dark matter, made of filaments connecting different clusters, all surrounded by voids. While its gravitational effects are observed by many probes, dark matter remains a mystery, with multiple experiments still ongoing to shed light on its nature (see e.g. Trimble 1987; Bertone et al. 2005; Buchmueller et al. 2017; de Swart et al. 2017, and references therein).

The most common tool to analyse and track the origin and evolution of dark matter structures are cosmological N -body simulations (Holmberg 1941; Navarro et al. 1996; Tormen 1997; Jenkins et al. 1998; Springel 2005; Springel et al. 2005; Boylan-Kolchin et al. 2009; Angulo et al. 2012; Villaescusa-Navarro et al. 2021, 2020; Chacón et al. 2020, and references therein). In its basic formulation, an N -body simulation is run by putting a certain number of massive particles in a cubic box, imposing periodic boundary conditions and letting gravity be the only force acting on the particles through its

gravitational potential, governed by the Poisson equation (Springel 2005). The initial conditions are usually described with a Gaussian density field, which can be entirely summarised by a given power spectrum, i.e. by the Fourier counterpart of the correlation function between different particles in the simulation. Starting from high redshift, the position and velocity of the particles are updated iteratively until today ($z = 0$), while various snapshots are taken at different redshifts.

Several methods to run an N -body simulation are available, with different levels of complexity, approximation, and speed (Hockney & Eastwood 1988; Chacón et al. 2020). These include the direct resolution of the equation of motion for each particle (Mikkola & Aarseth 1993), approximated methods like the tree code method (Barnes & Hut 1986; Callahan & Kosaraju 1992), or mean-field approaches like standard (Klypin & Holtzman 1997) or adaptive (O’Shea et al. 2004) particle mesh. In general, though, N -body simulations are computationally expensive to run, and usually require access to high performance computing hardware. This limits the possibility of fully exploring the impact of different cosmological parameters on the dark matter evolution in our Universe, and hinders statistical analyses of the large-scale structure (see e.g. Taylor et al. 2013; Taylor & Joachimi 2014): N -body simulations are essential to associate a covariance matrix to real measurements, and thousands of simulations are usually needed to obtain accurate estimates of such matrices.

In recent years, many cheaper approximations have been proposed,

* d.piras@ucl.ac.uk

which try to capture both the large-scale structure of the cosmic web and its smaller-scale details. These approximations often rely on Lagrangian perturbation theory (Buchert 1992; Buchert & Ehlers 1993; Buchert 1994), and can produce accurate dark matter halo mock catalogues and dark matter density fields (Monaco et al. 2002; Monaco et al. 2013; White et al. 2013; Kitaura et al. 2013; Chuang et al. 2014; Tassev et al. 2013; Tassev et al. 2015; Howlett et al. 2015; Rizzo et al. 2017; Tosone et al. 2020, 2021). While being capable of capturing the large-scale-structure statistics with fewer computational resources, these methods usually fail to accurately produce the correct small-scale statistics, and to date no inexpensive exact alternative to N -body simulations exists.

Another typical approximation to describe (dark) matter fields is found by resorting to a lognormal random field, which represents the simplest alternative to running an entire N -body simulation (Coles & Jones 1991; Peebles 1993; Taruya et al. 2002; Percival et al. 2004; Hilbert et al. 2011; Xavier et al. 2016). A lognormal random field can be easily obtained from a Gaussian random field (see Sect. 3.1 for further details), and can be entirely described by a small number of parameters; moreover, a lognormal variable has a skewed distribution which is suited for e.g. the matter overdensity field, whose values range from -1 in voids to values much higher than 1 in clustered dense regions. However, as reported in Xavier et al. (2016) and as shown in Fig. 1, the lognormal approximation comes with its own limitations, and fails to reproduce the correct matter density distribution especially at its tails.

Machine learning (ML) techniques have also been proposed to replace expensive N -body simulations. In Rodríguez et al. (2018), generative adversarial networks (GANs, Goodfellow et al. 2014) were successfully trained to generate slices of N -body simulations, and Mustafa et al. (2019) applied the same technique to weak lensing convergence maps. Perraudin et al. (2019) and Feder et al. (2020) then extended the application of GANs to 3-D boxes, proving that, while challenging to train, GANs can capture both large- and small-scale features, and are capable of accurately recovering the statistical information contained in the training data. He et al. (2019) and Alves de Oliveira et al. (2020), on the other hand, showed that it is possible to train a U-shaped neural network architecture (U-net, Ronneberger et al. 2015) to map simple linear initial conditions to the corresponding final evolved fields, correctly learning the non-linear growth of structures under the gravitational influence. Kaushal et al. (2021) additionally used Lagrangian perturbation theory to evolve such initial conditions and only learn the difference in the density fields at $z = 0$. In these latter works, it was also shown that such architectures can perform well even on input data obtained from different cosmological parameters than the training data, thus demonstrating the appealing feature of being able to extrapolate outside the training distribution. Other works have explored the use of super-resolution techniques to N -body simulations (Kodi Ramanah et al. 2020; Li et al. 2021), the application of normalising flows (e.g. Papamakarios et al. 2019) as generative models of the large-scale structure (Rouhiainen et al. 2021; Dai & Seljak 2022), wavelet phase harmonics statistics to produce realistic 2-D density fields (Allys et al. 2020), or combinations of ML-inspired techniques with more traditional methods to improve the accuracy of fast N -body solvers (Dai et al. 2018, 2020; Dai & Seljak 2021; Böhm et al. 2021).

While being useful, all the previous approaches still require a relatively high amount of computational resources, might not scale well to high-resolution fields, or introduce many approximations that prevent them from being used reliably in place of full N -body simulations. In this paper, we show that it is possible to improve the lognormal approximation by means of ML techniques, with the long-

term goal of integrating our approach with the *Full-sky Lognormal Astro-fields Simulation Kit* (FLASK, Xavier et al. 2016), in order to be able to cheaply generate more realistic high-resolution full-sky density fields.

For this purpose, we start from the Quijote N -body simulation suite (Villaescusa-Navarro et al. 2020), which offers thousands of realisations of a single cosmological parameterisation, as well as hundreds of simulations at different values of the cosmological parameters. We devise a pipeline to create lognormal density fields which are the approximated counterpart of the simulated density fields. By construction, these lognormal fields have the same power spectrum as the one from the fiducial N -body simulations, and the phases of the underlying Gaussian fields are taken from the initial conditions of the simulated fields (all details are reported in Sect. 3.1). Having the pairs of lognormal and corresponding simulated density fields, we draw from image-to-image translation techniques based on convolutional neural networks and adversarial training, in order to obtain a model that can map simple lognormal fields to more realistic density fields (see Fig. 1). We extensively validate our model by measuring first-, second-, and higher-order statistics, obtaining good agreement, almost always within 10%, on all scales. We additionally discuss how our model, despite being trained on a single set of cosmological parameters, can be successfully applied to slightly different cosmologies without re-training, while needing a more extensive study for different redshifts or cosmologies with bigger variations in the parameters.

The paper is structured as follows. In Sect. 2 we describe the Quijote simulation data, on which this work is based. In Sect. 3, we detail the procedure that we apply to obtain the training data, and describe the image-to-image translation technique that we employ in this work. In Sect. 4, we present the results for different resolutions of the density fields, as well as for different values of redshift and cosmological parameters, and demonstrate the performance of our model through a wide range of statistical tests. We conclude in Sect. 5 with a summary of our work, planned improvements and an outline of possible future applications of our model.

2 DATA

In this work, we use the Quijote simulation suite (Villaescusa-Navarro et al. 2020). This set of N -body simulations includes 15 000 realisations following 512^3 dark matter particles in a box with comoving length of $1 h^{-1}$ Gpc, with the matter density parameter $\Omega_m = 0.3175$, the baryon density parameter $\Omega_b = 0.049$, the Hubble parameter $h = 0.6711$, the scalar spectral index $n_s = 0.9624$, the root mean square of the matter fluctuations in spheres of radius $8 h^{-1}$ Mpc $\sigma_8 = 0.834$, and the dark energy equation of state parameter $w = -1$; neutrinos are considered massless. These simulations were run using the TreePM code Gadget-III, which is an improved version of Gadget-II (Springel 2005). We consider snapshots of both the initial conditions ($z = 127$) and today ($z = 0$), as well the $z = 1$ snapshot for further validation of our model (see Sect. 4.5).

In each N -body simulation, we convert the information on the particles' position to a continuous random field through a mass assignment scheme. We analyse the matter overdensity field $\delta(\mathbf{x})$, defined as:

$$\delta(\mathbf{x}) = \frac{\rho(\mathbf{x})}{\bar{\rho}} - 1, \quad (1)$$

with $\rho(\mathbf{x})$ being the matter density field at each position \mathbf{x} , and $\bar{\rho}$ being the mean density in the volume of the simulation.

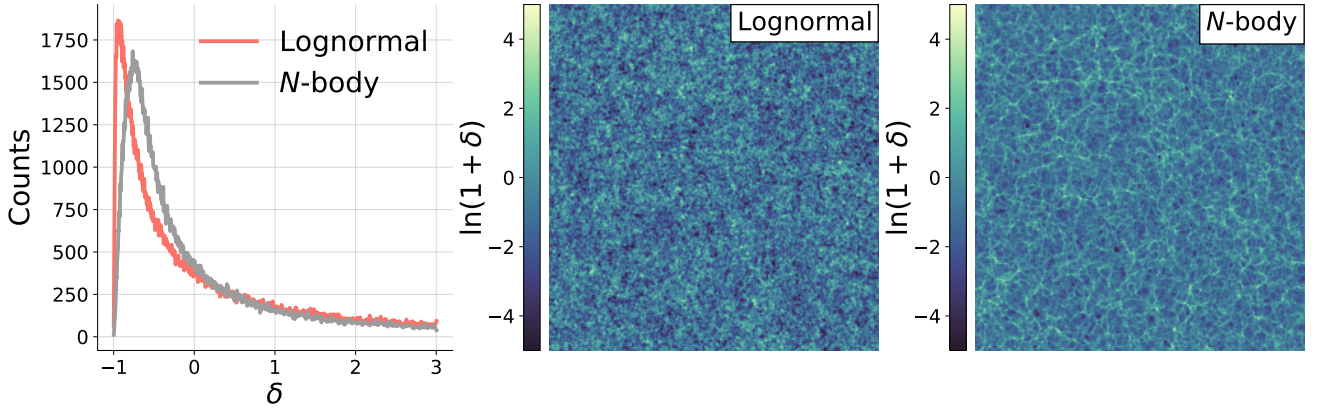


Figure 1. *Left panel:* histograms of the matter overdensity δ , defined in Eq. (1), for a lognormal random field (red) and an N -body simulation dark matter density field (grey). *Middle and right panels:* square maps of a lognormal (middle) and N -body (right) density fields, with a side of 512 pixels. In these maps, we clipped the maximum and minimum values before applying a logarithm to reduce their dynamic range; the symbol ‘ln’ indicates the natural logarithm throughout this paper. The right-hand-side plot is a slice of a simulation from the Quijote suite (Villaescusa-Navarro et al. 2020), while the middle plot, obtained following the procedure described in Sect. 3.1, represents its lognormal counterpart. The goal of this paper is to train a machine learning model (described in Sect. 3.2) to transform the lognormal map to the more realistic N -body map, thus improving the statistical power of the fast lognormal approximation.

Following Chaniotis & Poulidakos (2004); Jing (2005); Sefusatti et al. (2016), we consider a regular grid of points in all three directions. The continuous overdensity field is obtained by interpolating the discrete overdensity field on this grid, i.e. by evaluating the continuous function

$$\tilde{\delta}(\mathbf{x}) = \int \frac{d\mathbf{x}'}{(2\pi)^3} W(\mathbf{x} - \mathbf{x}') \delta(\mathbf{x}'), \quad (2)$$

with $W(\mathbf{x})$ being the weight function describing the number of grid points to which every particle is assigned. We choose the piecewise cubic spline interpolation scheme, i.e. we explicitly write the weight function as $W(\mathbf{x}) = W_{1D}(x_1/H)W_{1D}(x_2/H)W_{1D}(x_3/H)$, with H being the grid spacing, x_1 (x_2 , x_3) being the x (y , z) direction, and W_{1D} being the unidimensional weight function

$$W_{1D}(s) = \begin{cases} \frac{4-6s^2+3|s|^3}{6} & \text{if } 0 \leq |s| < 1; \\ \frac{(2-|s|)^3}{6} & \text{if } 1 \leq |s| < 2; \\ 0 & \text{otherwise;} \end{cases} \quad (3)$$

we refer the reader to Sefusatti et al. (2016) for more details. We consider both a grid with $N_{\text{high}}^3 = 512^3$ pixels and $N_{\text{low}}^3 = 128^3$ pixels, and present the results in Sect. 4.3 and Sect. 4.4, respectively.

3 METHOD

Our goal is to obtain 2-D projected density lognormal fields corresponding to slices of the Quijote simulations, in order to train a model that can take as input a lognormal map and predict a more realistic density field with the same statistics as the simulated one. In the following sections, we describe the procedure that we follow to obtain such a dataset (Sect. 3.1), and the machine learning algorithm that we employ to learn the transformation (Sect. 3.2).

3.1 Obtaining the training data

Since the long-term goal of the project is to increase the accuracy in large-scale structure description of random field maps on the sphere like the ones produced by FLASK (Xavier et al. 2016), we choose to work with slices of the density field rather than the full 3-D

boxes. We slice a given box along the third axis, and obtain multiple square density fields from a single simulation (128 in the low-resolution case, and 512 in the high-resolution case); the width of each slice is $1000 h^{-1} \text{ Mpc}/128 \simeq 7.8 h^{-1} \text{ Mpc}$ in the former case, and $1000 h^{-1} \text{ Mpc}/512 \simeq 1.9 h^{-1} \text{ Mpc}$ in the latter case. Since we consider 800 simulations in the low-resolution case, and 200 in the high-resolution case, we are left with 102 400 maps in both instances. We also consider the initial conditions of the 3-D boxes, namely the N -body simulations at $z = 127$, which we slice in the same way.

In order to create the lognormal counterpart of the more realistic maps, we start by measuring the power spectrum of each simulation’s slice at $z = 0$, which we wish to impose on the lognormal fields. We recall here that the 2-D matter power spectrum $P(k)$ can be implicitly defined through the Fourier transform $\delta(\mathbf{k})$ of the matter density contrast $\delta(\mathbf{x})$ ¹, defined as in Eq. (1):

$$\langle \delta(\mathbf{k})\delta(\mathbf{k}') \rangle = (2\pi)^2 P(k) \delta_D(\mathbf{k} + \mathbf{k}'), \quad (4)$$

where $\langle \cdot \rangle$ denotes an average over the whole Fourier space, $k = |\mathbf{k}|$, and $\delta_D(\cdot)$ indicates the Dirac delta function (Dodelson 2003); this in turn yields the estimator

$$\hat{P}(k) = \frac{1}{N_{\text{modes}}(k)} \sum_{|\mathbf{k}|=k} |\delta(\mathbf{k})|^2, \quad (5)$$

where $N_{\text{modes}}(k)$ is the number of modes in each k bin, and the sum is performed over all \mathbf{k} vectors whose magnitude is k . The definition in Eq. (4) implies that $P(k)$ is the Fourier counterpart of the 2-D matter correlation function $\xi(r)$, with $r = |\mathbf{r}|$, i.e.

$$P(k) = \int \xi(r) e^{-i\mathbf{k} \cdot \mathbf{r}} d^2 \mathbf{r}, \quad (6)$$

where $\xi(r)$ is defined as

$$\xi(r) = \langle \delta(\mathbf{x})\delta(\mathbf{x} + \mathbf{r}) \rangle, \quad (7)$$

with $\langle \cdot \rangle$ representing the average over all locations \mathbf{x} in the plane in this case.

In order to generate a lognormal random field with a given power spectrum, we follow the procedure of Coles & Jones (1991); Percival

¹ From now on, we use \mathbf{k} , \mathbf{x} and \mathbf{r} to indicate projected 2-D vectors.

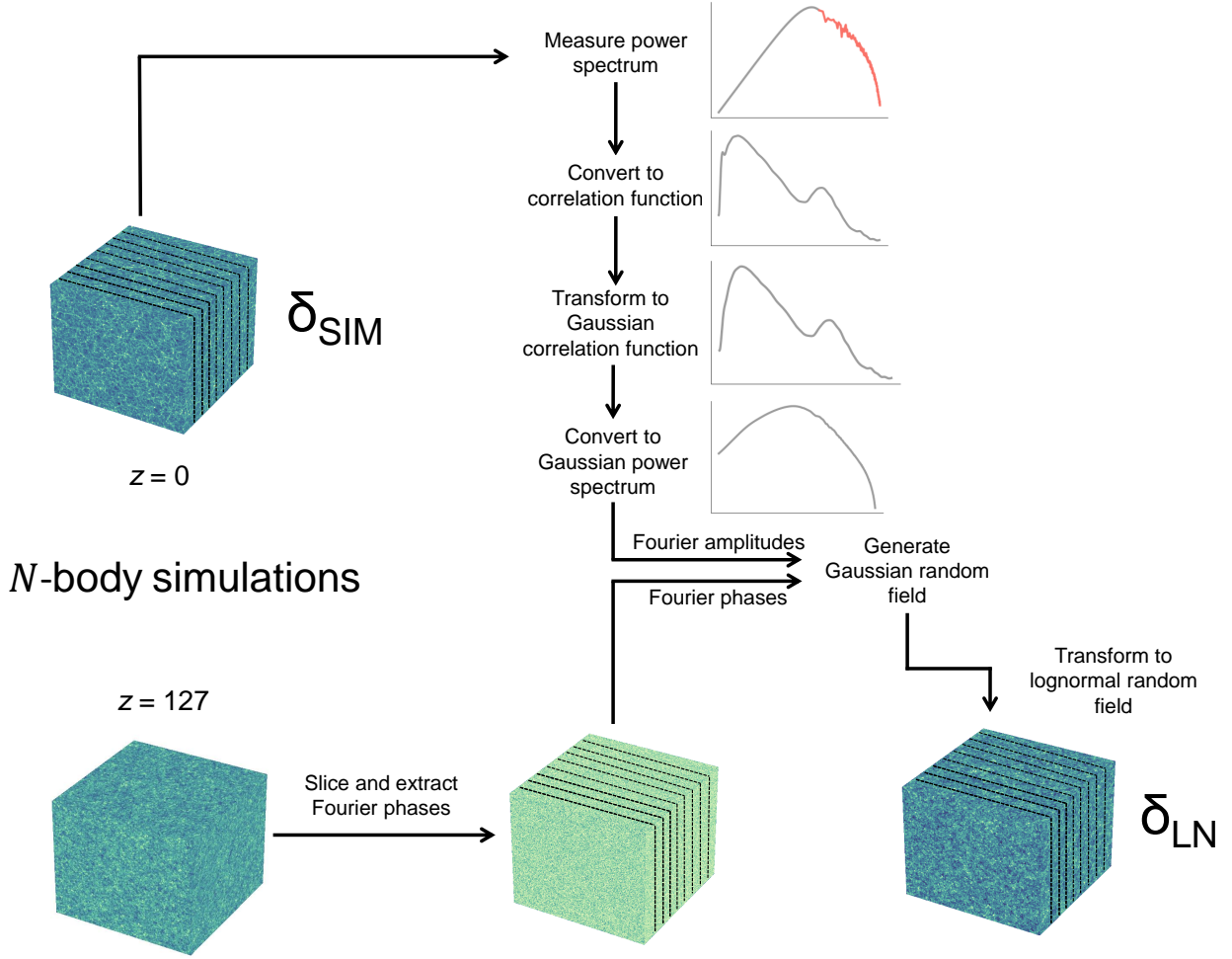


Figure 2. Flowchart of the steps to create the training data, as described in Sect. 3.1. We first measure the power spectrum of each slice of the $z = 0$ boxes (in red in the top panel), which is concatenated with the theory power spectrum obtained using CLASS (Blas et al. 2011; in grey in the top panel). We then generate a lognormal random field with this power spectrum, following Coles & Jones (1991); Percival et al. (2004). Crucially, when generating the underlying Gaussian field, we use the Fourier phases of the initial conditions of the *N*-body simulation, which consist of a Gaussian random field at $z = 127$. In this way, the lognormal field displays increased correlation with the *N*-body field. The final training data consists of pairs of lognormal (δ_{LN}) and simulated (δ_{SIM}) density fields, with either low (side $N_{\text{low}} = 128$) or high (side $N_{\text{high}} = 512$) resolution, as explained in Sect. 2. The machine learning model employed to learn the mapping from δ_{LN} to δ_{SIM} is presented in Sect. 3.2.

et al. (2004). We start by converting the measured power spectrum to the matter correlation function $\xi_{\text{LN}}(r)$, then we calculate the corresponding Gaussian correlation function,

$$\xi_{\text{G}}(r) = \ln [1 + \xi_{\text{LN}}(r)] , \quad (8)$$

transform it back to Fourier space and create a Gaussian random field realisation δ_{G} on a grid with this power spectrum and the required resolution (N_{low} or N_{high}). It is well known that a zero-mean Gaussian field is entirely specified by the given power spectrum, which only depends on the absolute value of the Fourier coefficients: this means that the Fourier phases can be uniformly sampled from the $[0, 2\pi]$ interval (Coles & Chiang 2000; Chiang & Coles 2000; Watts et al. 2003). Crucially, when generating the Gaussian random field, we employ the set of phases of the Gaussian initial conditions of the Quijote simulation realisation; in this way, the final lognormal density fields will have a high level of correlation with the density fields obtained from the simulations, especially on larger scales, as shown in Fig. 1. While the amount of correlation is limited due to the evolution from $z = 127$ to $z = 0$, we argue that our choice facil-

itates learning the skeleton of the large-scale structure: the Pearson correlation coefficient between pairs of maps can be as high as 0.5, if we smooth the fields with a Gaussian kernel on scales of about $50 h^{-1} \text{ Mpc}$, while it is consistent with 0 if using completely random phases.

Finally, we obtain the lognormal field δ_{LN} by calculating for each grid point

$$\delta_{\text{LN}} = \exp \left(\delta_{\text{G}} - \sigma_{\text{G}}^2 / 2 \right) - 1 \quad (9)$$

where σ_{G} is the standard deviation of the Gaussian field. For all these operations we employ the PYTHON package NBODYKIT (Hand et al. 2018). A flowchart representing the steps followed to produce the training data is reported in Fig. 2.

We observe two limitations due to the fact that we measure the power spectrum from a finite-resolution grid. First, by relying on the boxes only, we are capable of surveying only a limited range in k , namely no larger than $k \in [0.025 h \text{ Mpc}^{-1}, 1 h \text{ Mpc}^{-1}]$ in the high-resolution case, and $k \in [0.025 h \text{ Mpc}^{-1}, 0.3 h \text{ Mpc}^{-1}]$ in the low-

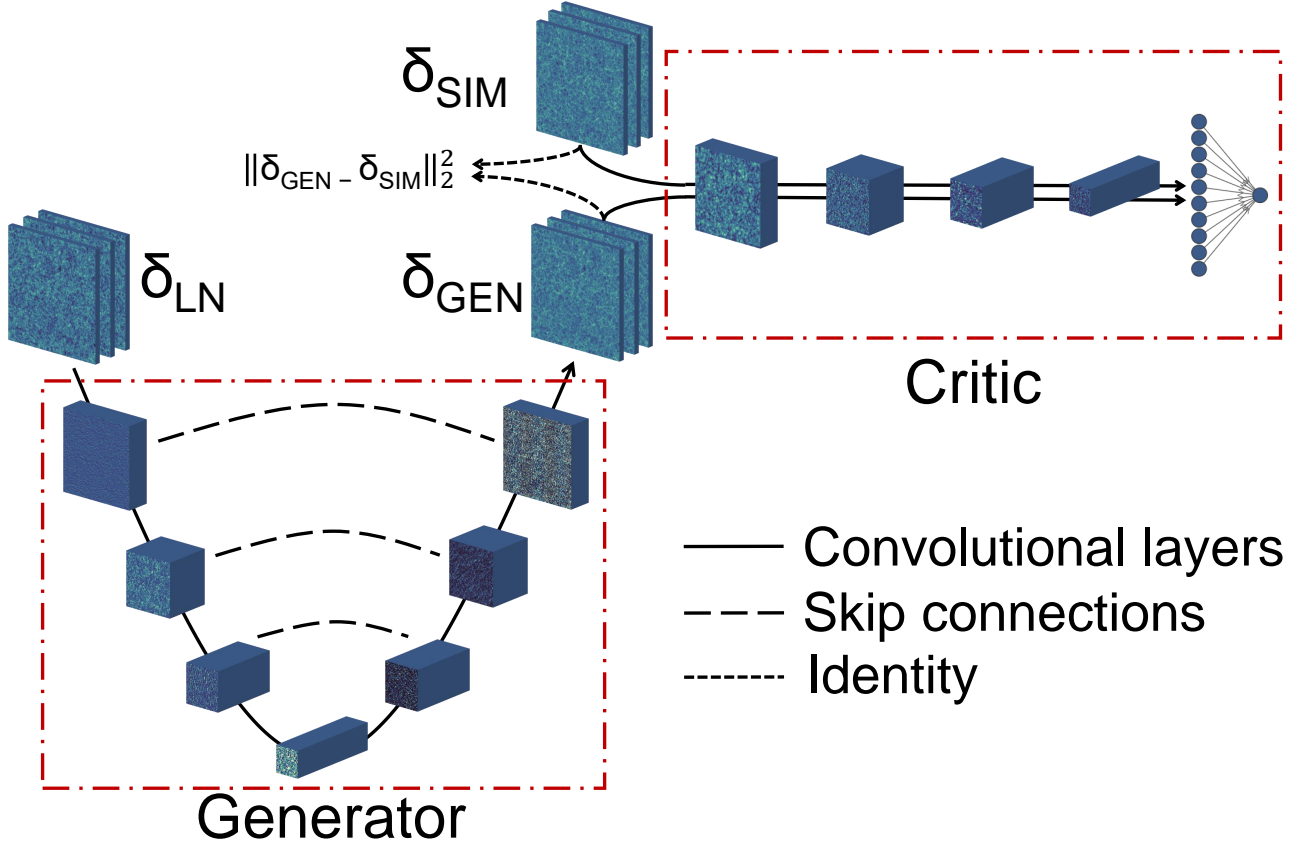


Figure 3. A representation of the generative model employed in this work, as described in Sect. 3.2. Following Isola et al. (2017), we have two convolutional neural networks, the generator (bottom left) and the critic (top right). We feed the lognormal maps through the generator, which is a U-net (Ronneberger et al. 2015), that first downsamples and then upsamples each image using various convolutional layers, with all details reported in Appendix A. To improve the performance of the model, each upsampling step is concatenated with the output of a downsampling step, as indicated by the dashed lines (*skip connections*). The output of the generator, dubbed δ_{GEN} , is then compared with the target data δ_{SIM} by the critic network, which is again made of various convolutional layers, ending with a dense layer in order to have a single output. The critic and generator networks are trained together, minimising the loss function of Eq. (10). Note that in addition to the standard adversarial loss, we include a penalty term in the form of the mean squared error between the generated and target maps, which we found to significantly improve the performance of our model; this is indicated by the short-dashed lines (*identity*).

resolution case. In order to access larger scales (i.e. lower k values), we concatenate the measured power spectrum with the theoretical one obtained with (CLASS Blas et al. 2011) for $k \in [10^{-5} h \text{ Mpc}^{-1}, 0.025 h \text{ Mpc}^{-1}]$: this makes the procedure outlined in the previous paragraphs more stable numerically.

Second, we observe a mismatch in power in the lognormal fields with respect to the imposed power spectrum. We attribute this discrepancy to the fact that when converting the Quijote initial conditions to a density field, the mass assignment scheme introduces extra spurious correlation in the phases, as well as to the noise arising from measuring the power spectrum on a slice of the density field, rather than the entire box. We correct for this effect, which is more pronounced at higher resolution, by iteratively rescaling the input power by the ratio of the output and target power at each k , until the mismatch across a sample of 100 random maps is smaller than 1% at all k values. We checked that this iterative adaptation scheme effectively removes the power mismatch, leaving the final performance of the model unaffected: the results presented in Sect. 4 do not change significantly if we use as input a slice of a 3-D lognormal field generated with completely random Fourier phases. We further remark that this correction would not be necessary if we had access to a perfectly Gaussian density field of the initial conditions.

We are left with pairs of square density field maps (dubbed δ_{LN} and

δ_{SIM}), which we use as the training (80%), validation (10%) and test (10%) data, further discussed in the next section. Note that to reduce the correlations between slices coming from the same simulation cube we shift the pixels by a random amount along both the first and second axis, independently for each pair of maps, assuming periodic boundary conditions. It could also be possible to randomly rotate and flip the slices in order to augment the training data; while we found it is not needed in our setup, we defer further investigations to future work. Before feeding the pairs into the neural network architecture described in the next section, we additionally preprocess each map by calculating $\ln(1 + \delta)$ to decrease the dynamic range of each density value δ .

3.2 Image-to-image translation

As discussed in Sect. 1, machine learning generative techniques have extensively been applied to N -body simulations. In this work, we aim at mapping lognormal fields to more realistic fields, hence we employ the *pix2pix* network structure, first proposed in Isola et al. (2017). The model is composed of two parts, as sketched in Fig. 3; all implementation details are reported in Appendix A. The first part is a U-net (Ronneberger et al. 2015), which takes as an input a lognormal map δ_{LN} , obtained and preprocessed as described in Sect. 3.1. The

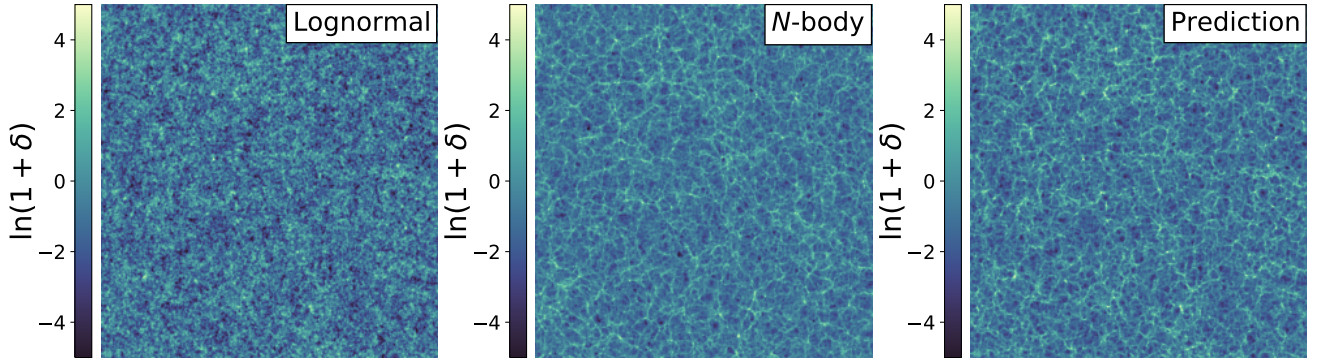


Figure 4. The lognormal (left) and N -body (middle) density fields as in Fig. 1, with the prediction of our model (right) given the lognormal field. In these maps, we clipped the maximum and minimum values before applying the logarithm to reduce their dynamic range. The model is described in Sect. 3.2. We remark that we are not interested in an exact match of the middle and right panels, as we explain in Sect. 4.1, and thoroughly test that the predicted fields carry the same statistical information as the N -body maps from Sect. 4.2.

map is passed through various convolutional layers to yield a compressed feature map, which is then upsampled back to the original resolution. Crucially, these upsampling steps are concatenated with the corresponding downsampled feature maps, which allow various scales to be accessible in the output map; removing these skip connections significantly impairs the performance of the model. We call the output map the *generated* map δ_{GEN} .

We want the generated map to carry the same statistical information as the δ_{SIM} density field. We tested that minimising a simple ℓ^1 or ℓ^2 norm between δ_{GEN} and δ_{SIM} is not sufficient to yield accurate results. For this reason, following Isola et al. (2017), we employ a second convolutional block as a discriminator, and express the loss in the framework of adversarial training. In the standard GAN framework (Goodfellow et al. 2014), the generator network G is trained together with the discriminator network D until an equilibrium where neither G or D can improve their performance is reached: while G attempts to generate realistic images, D tries to distinguish between real and fake examples. Since we found this framework to be particularly unstable during training, we actually implemented the Wasserstein GAN with gradient penalty (WGAN-GP, Arjovsky et al. 2017; Gulrajani et al. 2017), which we found superior both in performance and training stability. In this framework, a generator G is trained alongside a critic C to minimise the following cost function:

$$\mathbb{E}_{\delta_{\text{GEN}}} [C(\delta_{\text{GEN}})] - \mathbb{E}_{\delta_{\text{SIM}}} [C(\delta_{\text{SIM}})] + \lambda_1 \mathbb{E}_{\hat{\delta}} \left[\left(\|\nabla_{\hat{\delta}} C(\hat{\delta})\|_2 - 1 \right)^2 \right] + \lambda_2 \|\delta_{\text{GEN}} - \delta_{\text{SIM}}\|_2^2, \quad (10)$$

where $\delta_{\text{GEN}} = G(\delta_{\text{LN}})$, $\mathbb{E}_{\delta_{\text{GEN}}}$ and $\mathbb{E}_{\delta_{\text{SIM}}}$ indicate the expectation value over samples of the generated and simulated maps (usually estimated through sample averages), respectively, $\hat{\delta}$ represents a linear combination of δ_{GEN} and δ_{SIM} ², $\|\cdot\|_2$ indicates the ℓ^2 norm, and λ_1 and λ_2 are two positive hyperparameters that allow us to tune the amount of regularisation given by the gradient penalty and the ℓ^2 norm, respectively. In short, Eq. (10) indicates that we wish to minimise the Wasserstein-1 (or earth mover) distance between the real data and generated data distributions, while constraining the gradient of the critic network to be close to unity; this is needed since the

formulation of the Wasserstein distance as in the first two terms of Eq. (10) only holds when the critic is a 1-Lipschitz function, i.e. when its gradient is bound (see Gulrajani et al. 2017, for more details). We observe that in the standard WGAN-GP formulation $\lambda_2 = 0$, while in our case we found it key to minimise the ℓ^2 norm between simulated and generated maps as well in order to obtain improved results.

To train the networks, we use the Adam optimiser (Kingma & Ba 2014) with learning rate 10^{-5} ; we set the additional Adam hyperparameters $\beta_1 = 0$ and $\beta_2 = 0.9$, following Gulrajani et al. (2017), and refer the reader to Kingma & Ba (2014) and Gulrajani et al. (2017) for more details. We feed the data in batches of 32 pairs at each iteration, and train our model for 10 epochs, where each epoch consists of feeding the entire training set through the network. For each batch, we update the critic parameters 10 times, and the generator parameters only once. Each epoch takes about 1 h (8 h) for the low (high) resolution case, on a Tesla P100 GPU; after training, mapping a lognormal map through the generator takes $\mathcal{O}(1 \text{ s})$ on the same hardware, and can be efficiently done in batches.

We save the model after each epoch. In order to select the best model amongst the saved ones, for each of them we run the statistical tests described in Sect. 4.2, and measure the mean percentage difference between the target and predicted maps for randomly-sampled maps of the validation set. The best model is chosen as the one which minimises the sum of the mean percentage differences over all tests; the results are then shown on maps from the test set. In the high resolution case, we actually found that the trained model generates some maps whose power spectrum is significantly different from the input and target ones, which we attribute to instabilities of the WGAN-GP framework. For this reason, we take all the predictions from the test set, and we rank them based on the mean difference between the input power spectrum and the predicted power spectrum; we select the best 30 maps according to this metric, and discuss possible ways to make the model more stable in Sect. 5.

We show the results of our best models in the next section. These models are found with $\lambda_1 = 100$ and $\lambda_2 = 10$; we defer a full grid search over these hyperparameters to future work.

4 RESULTS

In this section, we validate the performance of the trained model by comparing the statistics of the generated and simulated maps.

² In particular, $\hat{\delta} = \delta_{\text{SIM}} + u(\delta_{\text{GEN}} - \delta_{\text{SIM}})$, with $u \sim U(0, 1)$, where $U(0, 1)$ indicates the uniform distribution between 0 and 1. This linear combination means that we are constraining the gradient norm to be 1 only along lines connecting real and fake data, which should be sufficient to guarantee good experimental results (Gulrajani et al. 2017).

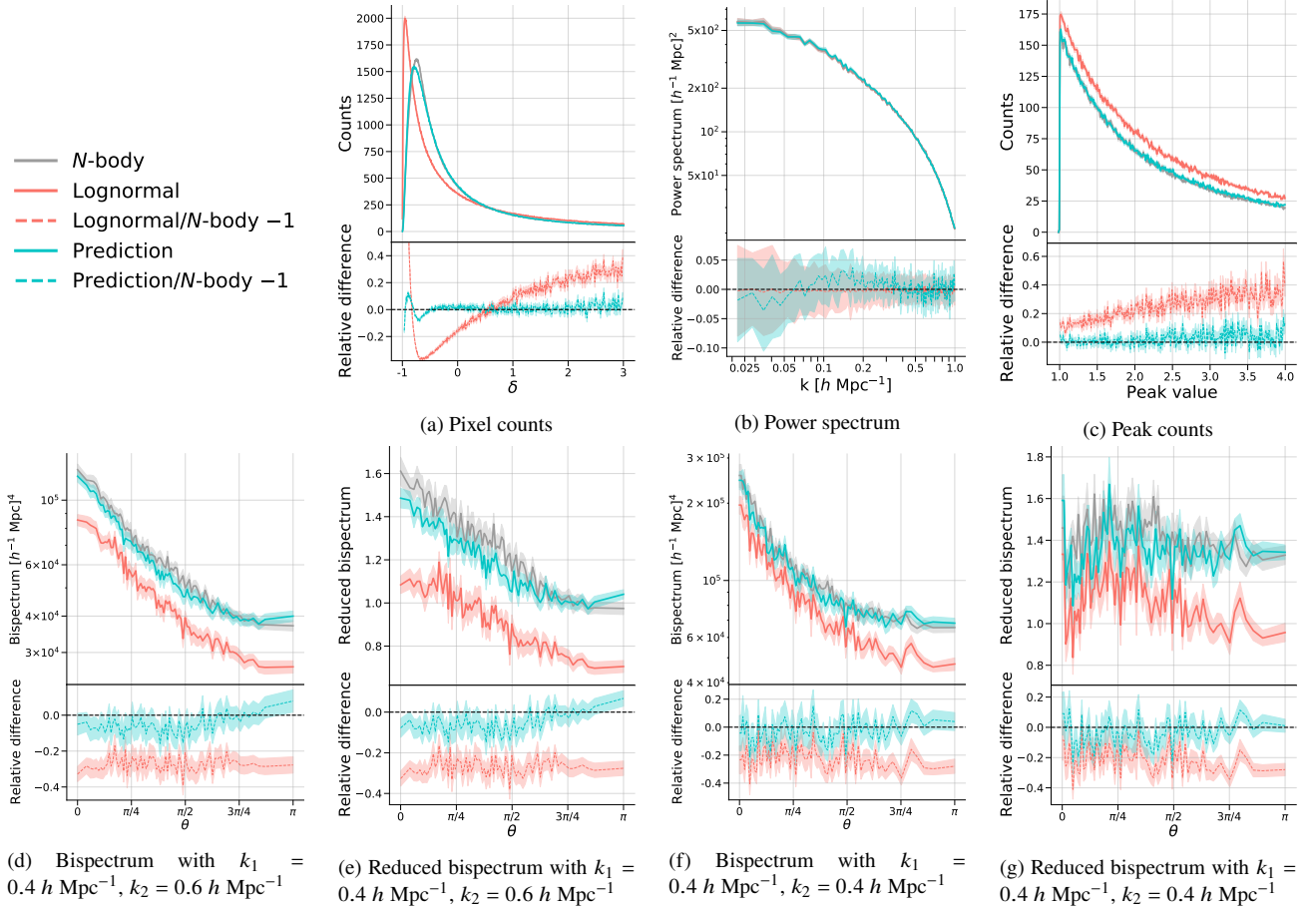


Figure 5. Comparison of the statistical tests described in Sect. 4.2 for the lognormal (δ_{LN} , in red), N -body (δ_{SIM} , in grey), and predicted (δ_{GEN} , in cyan) maps, considering a resolution of $N_{\text{high}} = 512$. The performance is measured at the bottom of each panel by calculating the relative difference of N -body against predicted and lognormal maps (dashed lines). All solid lines indicate the mean values over 30 maps, and the error bars represent the error on the mean (or propagated error, in the case of the relative differences). We observe that, except for the range $-1 < \delta < 0$ in panel (a) and some individual θ values in panels (d)–(g), the prediction always matches the target statistics within the error bars, performing significantly better than the lognormal approximation.

4.1 Qualitative comparison

While the appearance of the maps is irrelevant for the purpose of our statistical analysis, a visual inspection is nonetheless useful to intuitively understand whether our model is on the right track to learn the N -body features. In Fig. 4, we show a lognormal map, its N -body counterpart and the prediction of our model given the lognormal map for the high-resolution case.

Our goal is not to obtain an exact visual match between the model’s prediction and the N -body map, given that we used the random phases of the $z = 127$ simulations, which only have partial correlations with the $z = 0$ slices. For the applications we focus on (discussed in Sect. 5), the actual position of peaks and voids in the lognormal map is irrelevant, since it is dictated by the random sampling of the phases: we only aim to generate maps which carry the same statistical signal as the N -body maps on average, improving on the lognormal approximation. We observe that while the predicted field does not match the N -body pattern pixel by pixel, the model has learnt the correct morphology of the large-scale structure on top of the lognormal field.

4.2 Statistics

While visual inspection of the generated maps against the target ones is a necessary zeroth-order test to provide intuition on whether the model was adequately trained, it is then fundamental to compare the summary statistics of interests and carefully quantify their agreement. We compare the generated and simulated fields through four different summary statistics, which we briefly describe here.

4.2.1 Pixel counts

The first test consists of binning the pixels of the generated and target density fields into a histogram. While the lognormal distribution is a good approximation of the simulated fields, there is a significant difference between the two, especially at the tails of the density values (see e.g. Fig. 1). We show in panel (a) of Fig. 5 and Fig. 6 the performance of our model with respect to the pixel counts for high and low resolution, respectively.

4.2.2 Power spectrum

We compare the power spectrum as defined in Eq. (4) for the simulated maps and the ones predicted by our model given the lognormal maps. While it could be argued that this is a trivial task (given that the

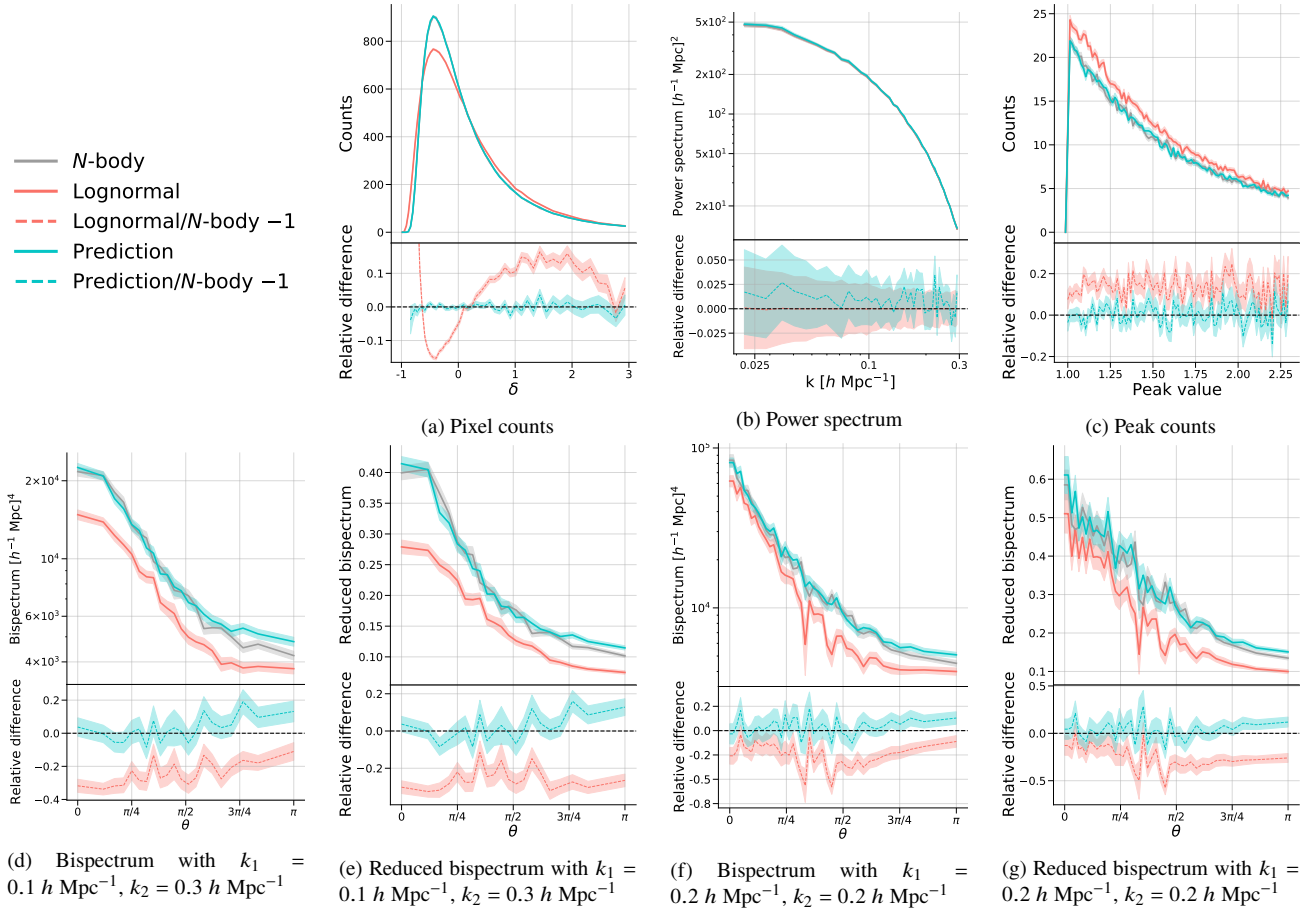


Figure 6. Same as Fig. 5, with a lower field resolution $N_{\text{low}} = 128$. In this case, the solid lines indicate the mean values over 100 maps. We observe that the model's performance is almost always within the 5% range, except for the bispectra, where significant differences are present at high θ ; we discuss these discrepancies in Sect. 4.4. Despite these differences, our model still outperforms the lognormal approximation.

input and output maps have the same power spectrum by construction), it is not obvious that our model does not modify the power spectrum information while learning the new density distribution, and as anticipated at the end of Sect. 3.2 we actually found some failures of the trained model which yield discrepant power spectra in the high-resolution case. We therefore show the power spectra and the results in panel (b) of Fig. 5 and Fig. 6, for high and low resolution, respectively.

4.2.3 Bispectrum

To probe the non-Gaussian features of the density fields, we measure the matter bispectrum of the maps, i.e. the counterpart of the three-point matter correlation function in Fourier space. The matter bispectrum $B(k_1, k_2, k_3)$ for a 2-D field is defined implicitly as (see e.g. Sefusatti et al. 2006):

$$\langle \delta(\mathbf{k}_1) \delta(\mathbf{k}_2) \delta(\mathbf{k}_3) \rangle = (2\pi)^2 \delta_D(\mathbf{k}_1 + \mathbf{k}_2 + \mathbf{k}_3) B(k_1, k_2, k_3), \quad (11)$$

where $\delta(\mathbf{k})$ indicates the Fourier transform of the matter overdensity $\delta(\mathbf{x})$, $k_i = |\mathbf{k}_i|$, and all \mathbf{k}_i vectors are in the plane of the simulation box slices. To further assess that our model correctly captured the information beyond the power spectrum, we also measure the reduced matter bispectrum $Q(k_1, k_2, k_3)$, see e.g. Liguori et al. (2010), defined as:

$$Q(k_1, k_2, k_3) = \frac{B(k_1, k_2, k_3)}{P(k_1)P(k_2) + P(k_1)P(k_3) + P(k_2)P(k_3)}. \quad (12)$$

We measure bispectra and reduced bispectra for different configurations depending on the resolution; different triangle configurations usually probe different inflationary models (Liguori et al. 2010), and one must include as many configurations as possible to break degeneracies when inferring cosmological parameters (Bergé et al. 2010). Moreover, different bispectra configurations can shed light on the size of collapsing regions, as well as on the relative position of clusters and voids in the large-scale structure (Munshi et al. 2020).

We calculate bispectra and reduced bispectra based on an estimator of the binned bispectrum (see e.g. Bucher et al. 2016); we consider the centroid of each bin as the value of \mathbf{k} at which the bispectrum is evaluated. We report the results in panels (d)–(g) of Fig. 5 and Fig. 6 (for high and low resolution, respectively) as a function of the angle θ between the vectors \mathbf{k}_1 and \mathbf{k}_2 .

4.2.4 Peak counts

To further assess whether the model has correctly learnt the most non-Gaussian features of the simulated density fields, we verify that the peak counts of the generated and target maps match within the error bars. A peak is defined as a density pixel which is higher than the 8 surrounding pixels. Peak count statistics have been shown to carry significant cosmological information, especially in weak lensing studies, as they trace the most dense regions (Pires et al. 2009, 2012; Dietrich & Hartlap 2010; Marian et al. 2011; Mainini & Romano 2014; Lin & Kilbinger 2015a,b; Lin et al. 2016; Kacprzak

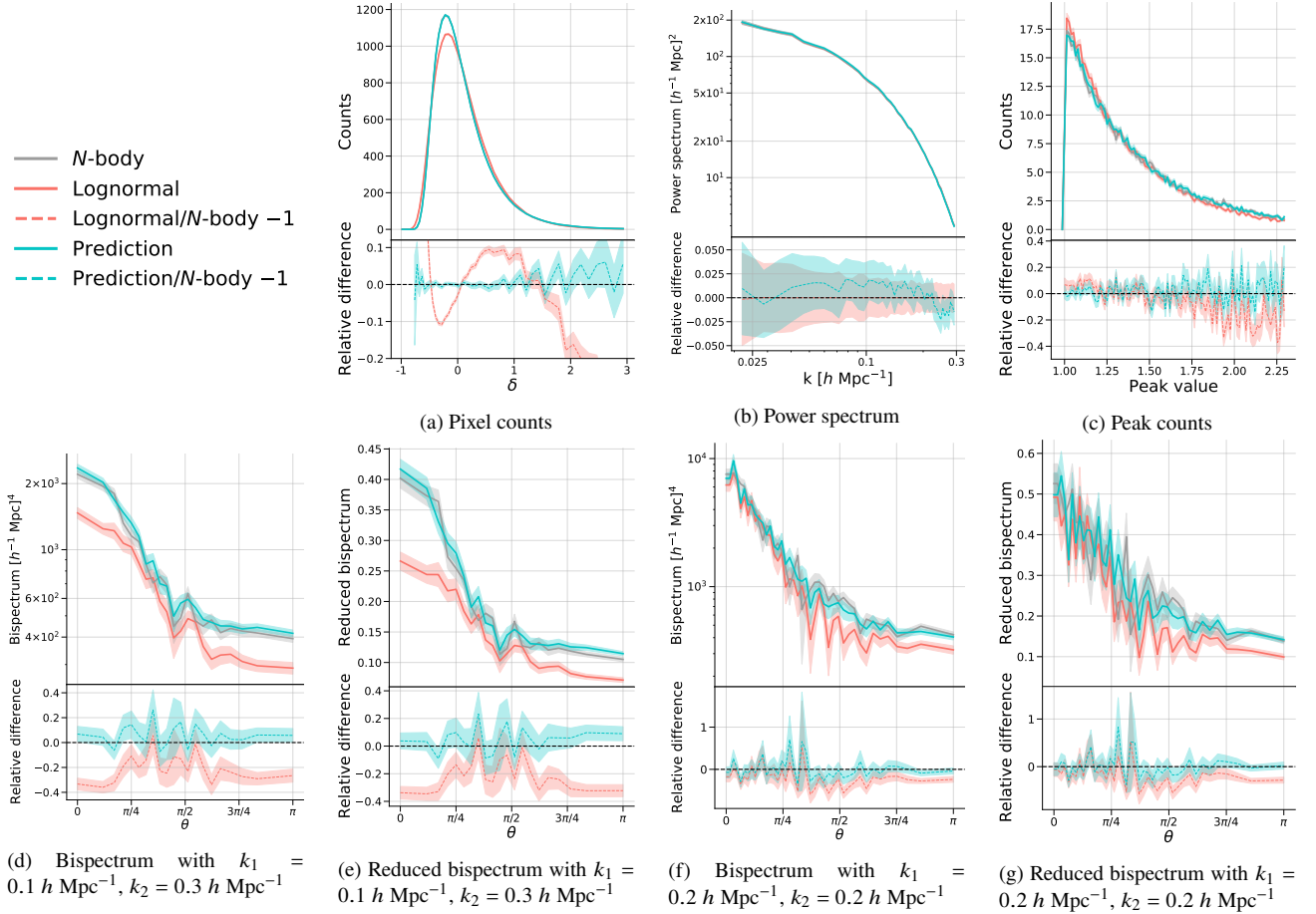


Figure 7. Same as Fig. 6, for a different model trained on data at redshift $z = 1$. We observe a good overall performance of our model, which generally outperforms the lognormal approximation.

et al. 2016; Shan et al. 2018; Martinet et al. 2018; Harnois-Déraps et al. 2021). We bin the peak values for both the simulated and target maps, and compare them in panel (c) of Fig. 5 and Fig. 6, for high and low resolution, respectively.

4.3 High resolution

In Fig. 5 we compare the performance of the predictions of our model against the target maps, for the case with 512^2 pixels. We run the statistical tests on 30 maps sampled from the test set as described at the end of Sect. 3.2; the solid lines show the mean values and the dashed areas represent the error on the mean.

In panel (b), we show that the trained model is capable of preserving the correct power spectrum on all scales from $0.025 h \text{ Mpc}^{-1}$ to $1 h \text{ Mpc}^{-1}$, with percentage differences going no higher than 5%, and always within the error bars. At the same time, the model correctly improves on the lognormal approximation as far as the peak counts and pixel counts are concerned, with significant differences for $-1 < \delta < 0$ in the latter case only. We believe that the performance in this case could be ameliorated by e.g. exploring different network architectures. In panels (d)-(g), we show the results for the (reduced) bispectrum, for $k_1 = 0.4 h \text{ Mpc}^{-1}$, $k_2 = 0.6 h \text{ Mpc}^{-1}$ — panels (d) and (e) — and for $k_1 = 0.4 h \text{ Mpc}^{-1}$, $k_2 = 0.4 h \text{ Mpc}^{-1}$ — panels (f) and (g). The performance is very good overall, with the percentage difference between target and predicted maps being within the error

bars except for a few individual values of θ , significantly improving on the lognormal approximation.

4.4 Low resolution

In Fig. 6 we compare the performance of the predictions of our model against the target maps, for the case with 128^2 pixels. In this case, we use 100 randomly-sampled maps from the test set. We observe good agreement between predicted and target maps for the pixel counts, power spectrum and peak counts statistics, with the power spectrum in particular being almost always within 2%. As far as the bispectra are concerned, we consider two configurations, one with $k_1 = 0.1 h \text{ Mpc}^{-1}$, $k_2 = 0.3 h \text{ Mpc}^{-1}$ — panels (d) and (e) — and for $k_1 = 0.2 h \text{ Mpc}^{-1}$, $k_2 = 0.2 h \text{ Mpc}^{-1}$ — panels (f) and (g). Since the fields have a lower resolution, the scales we probe are larger than in Sect. 4.3. We observe a good agreement overall, except at high θ : we argue that to improve the performance of the model we could use the same ranking approach based on the power spectrum as in the high-resolution case.

4.5 Redshift and cosmology dependence

So far, we have shown the performance of our model on a given fiducial set of cosmological parameters and redshift, from which the training data were obtained. However, in order for the method to become practical, it is critical to assess whether the performance

degrades when the model is tested on lognormal maps obtained with a different cosmology or at different z . Examples of good generalisation properties of machine learning models applied to cosmological problems include He et al. (2019); Kaushal et al. (2021); Shao et al. (2022).

We checked that the performance of our model does not degrade much when acting on fields with slightly different (within 2%) values of Ω_m and σ_8 , even though a more complete analysis on bigger variations is required. We additionally verified that feeding our model, trained using maps at $z = 0$, with lognormal maps at $z = 0.5$ or $z = 1.0$ does not yield satisfactory results, with percentage errors going well above 50%. This failure is not unexpected: the different dynamic range of the lognormal maps at different redshifts highlights that our model is not capable of extrapolating to such different input values.

To overcome these limitations, one possible solution is to normalise the maps, either after or before training the model. For instance, one could rescale the field at $z = 1$ through the linear growth factor (Eisenstein et al. 1999) to $z = 0$, and then invert this transformation after feeding the map through the generator trained as above. However, this approach would ignore the non-linear scales, and directly dividing each pixel value by the linear growth factor could lead to unphysical fields with $\delta < -1$. Alternatively, instead of the dark matter overdensity field, we could consider the corresponding peak height field, calculated by measuring for each pixel $1.686/\sigma(M)$, where $\sigma(M)$ is the mass enclosed within a given scale; since the peak height is known to extrapolate better, having a weaker dependence on cosmological parameters (Press & Schechter 1974; Bond et al. 1991; Percival 2005; Kravtsov & Borgani 2012), we expect a model trained on this field to have an improved generalisation performance.

Moreover, we can actually show that with our current setup we can successfully train a second model on data generated as described in Sect. 3.1 with $z \neq 0$. We show the results for a model trained on fields at $z = 1$, which have a lower contrast and less non-linearity than $z = 0$, in Fig. 7 for the low-resolution case, with good performance overall. We also expect that it would be possible to train a conditional model by providing the redshift or cosmology ‘label’ together with the input lognormal map, thus obtaining a conditional WGAN-GP (see e.g. Mirza & Osindero 2014; Yiu et al. 2021); such a model could be trained e.g. on maps with $z = 0$ and $z = 1$, and then used to predict maps at $z = 0.5$, similarly to Chen et al. (2020). All these points indicate that it will be possible to make our model conditional on z and different cosmological parameter; we defer these studies to future work.

5 CONCLUSIONS

In this paper, we employed the Quijote simulations as a starting point to train a machine learning model that is capable of transforming projected lognormal realisations of the dark matter density field to more realistic samples of the dark matter distribution. We employed state-of-the-art image-to-image translation techniques, combining convolutional neural networks and adversarial training, to learn such a model, and extensively validated its performance through a thorough set of statistical tests. We observed a significant reduction in the error of non-Gaussian features like peak counts and bispectra, from tens of percent for the pure lognormal model to no more than 10% obtained by our model in most cases; the latter frequently shows an order of magnitude improvement over the former. Furthermore, the mapping is extremely fast, taking $O(1\text{ s})$.

We mainly focused on a fiducial cosmology and a single redshift value; however, in order to avoid running large suites of N -body simulations, the proposed method has to generalise well to other redshifts and cosmologies. We verified that there is room for improvement when applying our model to different redshift values and significant variations in the cosmological parameters, and we outlined a few promising avenues to investigate in order to overcome these issues. While in this work we trained different models for different resolutions of the density field, we also expect an improved model to be able to deal with a varying slice thickness.

We plan to extend this work to random fields on the sphere, and integrate it into the FLASK package developed in Xavier et al. (2016). We aim to extend our approach to spherical random fields by iteratively applying our model to square patches of the sky, thus providing the community with a tool to quickly generate realistic dark matter realisations that overcome the limitations of the lognormal approximation. We also plan to compare our approach to a direct generation of spherical fields by means of spherical convolutional layers, as proposed e.g. for mass maps in Yiu et al. (2021).

Additionally, we believe that the procedure outlined in this paper could be applied to augment analytical approximations to N -body simulations (like L-PICOLA, Howlett et al. 2015, or FastPM, Feng et al. 2016), as well as semi-analytical models of galaxies, which, in the same vein as lognormal random fields, provide a fast approximation to hydrodynamical simulations by modelling complicated baryonic processes (White & Frenk 1991; Kauffmann et al. 1993; Cole et al. 1994; Somerville & Primack 1999; Lacey 2001). We further plan to explore the possibility to employ the dataset described in this work to reduce the variance in the statistics of large-scale structure observables using a small number of expensive simulations (Chartier et al. 2021; Chartier & Wandelt 2021; Ding et al. 2022), as well as to replace our WGAN-GP model with either a possibly more stable GAN version (Kwon et al. 2021), or with a more compact model, like the one proposed in the context of Lagrangian deep learning (LDL, Dai & Seljak 2021), using graph neural networks (GNNs, see e.g. Zhou et al. 2018 for a review) or through normalising flows (e.g. FFJORD, Grathwohl et al. 2018, or more recently TREN, Dai & Seljak 2022). This will be investigated in future work.

ACKNOWLEDGEMENTS

We thank Ofer Lahav, Shirley Ho, John Shawe-Taylor and Ilya Feige for useful discussion and feedback on this work. DP thanks William Coulton and Susan Pyne for their help with the bispectrum estimation. DP was supported by the STFC UCL Centre for Doctoral Training in Data Intensive Science. This work has been partially enabled by funding from the UCL Cosmoparticle Initiative. We acknowledge the use of NUMPY (Harris et al. 2020), MATPLOTLIB (Hunter 2007), TENSORFLOW (Abadi et al. 2015), and NN-SVG (LeNail 2019).

DATA AVAILABILITY

The original data underlying this article (i.e. the Quijote simulations) are available through the *globus* server, as detailed in the documentation at this link. The byproduct data obtained for this work will be shared on reasonable request to the corresponding author. The code to reproduce this work will be shared upon acceptance of the paper.

REFERENCES

- Abadi M., et al., 2015, TensorFlow: Large-Scale Machine Learning on Heterogeneous Systems, <http://tensorflow.org/>
- Allys E., Marchand T., Cardoso J. F., Villaescusa-Navarro F., Ho S., Mallat S., 2020, *Phys. Rev. D*, **102**, 103506
- Alves de Oliveira R., Li Y., Villaescusa-Navarro F., Ho S., Spergel D. N., 2020, arXiv e-prints, [p. arXiv:2012.00240](https://arxiv.org/abs/2012.00240)
- Angulo R. E., Springel V., White S. D. M., Jenkins A., Baugh C. M., Frenk C. S., 2012, *MNRAS*, **426**, 2046
- Arjovsky M., Chintala S., Bottou L., 2017, arXiv e-prints, [p. arXiv:1701.07875](https://arxiv.org/abs/1701.07875)
- Barnes J. E., Hut P., 1986, *Nature*, **324**, 446–449
- Bergé J., Amara A., Réfrégier A., 2010, *The Astrophysical Journal*, **712**, 992
- Bertone G., Hooper D., Silk J., 2005, *Physics Reports*, **405**, 279–390
- Blas D., Lesgourgues J., Tram T., 2011, *Journal of Cosmology and Astroparticle Physics*, **2011**, 034
- Böhm V., Feng Y., Lee M. E., Dai B., 2021, *Astronomy and Computing*, **36**, 100490
- Bond J. R., Cole S., Efstathiou G., Kaiser N., 1991, *ApJ*, **379**, 440
- Boylan-Kolchin M., Springel V., White S. D. M., Jenkins A., Lemson G., 2009, *Monthly Notices of the Royal Astronomical Society*, **398**, 1150
- Bucher M., Racine B., van Tent B., 2016, *J. Cosmology Astropart. Phys.*, **2016**, 055
- Buchert T., 1992, *Monthly Notices of the Royal Astronomical Society*, **254**, 729
- Buchert T., 1994, *Monthly Notices of the Royal Astronomical Society*, **267**, 811–820
- Buchert T., Ehlers J., 1993, *Monthly Notices of the Royal Astronomical Society*, **264**, 375
- Buchmueller O., Doglioni C., Wang L.-T., 2017, *Nature Physics*, **13**, 217–223
- Callahan P. B., Kosaraju S. R., 1992, in Proceedings of the Twenty-Fourth Annual ACM Symposium on Theory of Computing. STOC '92. Association for Computing Machinery, New York, NY, USA, p. 546–556, [doi:10.1145/129712.129766](https://doi.org/10.1145/129712.129766), <https://doi.org/10.1145/129712.129766>
- Chacón J., Vázquez J. A., Gabbasov R., 2020, *Revista Mexicana de Física E*, **17**, 241–254
- Chaniotis A. K., Poulikakos D., 2004, *Journal of Computational Physics*, **197**, 253
- Chartier N., Wandelt B. D., 2021, arXiv e-prints, [p. arXiv:2106.11718](https://arxiv.org/abs/2106.11718)
- Chartier N., Wandelt B. D., Akrami Y., Villaescusa-Navarro F., 2021, *Monthly Notices of the Royal Astronomical Society*, **503**, 1897–1914
- Chen C., Li Y., Villaescusa-Navarro F., Ho S., Pullen A., 2020, arXiv e-prints, [p. arXiv:2012.05472](https://arxiv.org/abs/2012.05472)
- Chiang L.-Y., Coles P., 2000, *Monthly Notices of the Royal Astronomical Society*, **311**, 809–824
- Chuang C.-H., Kitaura F.-S., Prada F., Zhao C., Yepes G., 2014, *Monthly Notices of the Royal Astronomical Society*, **446**, 2621–2628
- Cole S., Aragon-Salamanca A., Frenk C. S., Navarro J. F., Zepf S. E., 1994, *MNRAS*, **271**, 781
- Coles P., Chiang L.-Y., 2000, *Nature*, **406**, 376–378
- Coles P., Jones B., 1991, *MNRAS*, **248**, 1
- Dai B., Seljak U., 2021, *Proceedings of the National Academy of Sciences*, **118**, e2020324118
- Dai B., Seljak U., 2022, arXiv e-prints, [p. arXiv:2202.05282](https://arxiv.org/abs/2202.05282)
- Dai B., Feng Y., Seljak U., 2018, *Journal of Cosmology and Astroparticle Physics*, **2018**, 009–009
- Dai B., Feng Y., Seljak U., Singh S., 2020, *Journal of Cosmology and Astroparticle Physics*, **2020**, 002–002
- Dietrich J. P., Hartlap J., 2010, *Monthly Notices of the Royal Astronomical Society*, **402**, 1049
- Ding Z., et al., 2022, arXiv e-prints, [p. arXiv:2202.06074](https://arxiv.org/abs/2202.06074)
- Dodelson S., 2003, *Modern Cosmology*. Academic Press, San Diego, CA, <https://cds.cern.ch/record/1282338>
- Dumoulin V., Visin F., 2016, arXiv e-prints, [p. arXiv:1603.07285](https://arxiv.org/abs/1603.07285)
- Eisenstein D. J., Hu W., Tegmark M., 1999, *ApJ*, **518**, 2
- Feder R. M., Berger P., Stein G., 2020, *Physical Review D*, **102**
- Feng Y., Chu M.-Y., Seljak U., McDonald P., 2016, *Monthly Notices of the Royal Astronomical Society*, **463**, 2273–2286
- Fukushima K., 1980, *Biological Cybernetics*, **36**, 193
- Glorot X., Bordes A., Bengio Y., 2011, in Gordon G., Dunson D., Dudík M., eds, Proceedings of Machine Learning Research Vol. 15, Proceedings of the Fourteenth International Conference on Artificial Intelligence and Statistics. PMLR, Fort Lauderdale, FL, USA, pp 315–323, [http://proceedings.mlr.press/v15/glorot11a.html](https://proceedings.mlr.press/v15/glorot11a.html)
- Goodfellow I. J., Pouget-Abadie J., Mirza M., Xu B., Warde-Farley D., Ozair S., Courville A., Bengio Y., 2014, in Proceedings of the 27th International Conference on Neural Information Processing Systems - Volume 2. NIPS'14. MIT Press, Cambridge, MA, USA, p. 2672–2680
- Goodfellow I., Bengio Y., Courville A., 2016, *Deep Learning*. MIT Press, <http://www.deeplearningbook.org>
- Grathwohl W., Chen R. T. Q., Bettencourt J., Sutskever I., Duvenaud D., 2018, arXiv e-prints, [p. arXiv:1810.01367](https://arxiv.org/abs/1810.01367)
- Gulrajani I., Ahmed F., Arjovsky M., Dumoulin V., Courville A. C., 2017, *CoRR*, abs/1704.00028
- Hand N., Feng Y., Beutler F., Li Y., Modi C., Seljak U., Slepian Z., 2018, *The Astronomical Journal*, **156**, 160
- Harnois-Déraps J., Martinet N., Castro T., Dolag K., Giblin B., Heymans C., Hildebrandt H., Xia Q., 2021, *MNRAS*, **506**, 1623
- Harris C. R., et al., 2020, *Nature*, **585**, 357
- He S., Li Y., Feng Y., Ho S., Ravanbakhsh S., Chen W., Póczos B., 2019, *Proceedings of the National Academy of Sciences*, **116**, 13825–13832
- Hilbert S., Hartlap J., Schneider P., 2011, *A&A*, **536**, A85
- Hockney R. W., Eastwood J. W., 1988, Computer simulation using particles. Bristol: Hilger, 1988, <https://www.bibsonomy.org/bibtex/26f9933cf106eac0cb4d51d96072a709a/pkilian>
- Holmberg E., 1941, *ApJ*, **94**, 385
- Howlett C., Manera M., Percival W. J., 2015, *Astronomy and Computing*, **12**, 109
- Hunter J. D., 2007, *Computing in Science & Engineering*, **9**, 90
- Ioffe S., Szegedy C., 2015, arXiv e-prints, [p. arXiv:1502.03167](https://arxiv.org/abs/1502.03167)
- Isola P., Zhu J.-Y., Zhou T., Efros A. A., 2017, in 2017 IEEE Conference on Computer Vision and Pattern Recognition (CVPR). pp 5967–5976, [doi:10.1109/CVPR.2017.632](https://doi.org/10.1109/CVPR.2017.632)
- Jenkins A., et al., 1998, *ApJ*, **499**, 20
- Jing Y. P., 2005, *The Astrophysical Journal*, **620**, 559–563
- Kacprzak T., et al., 2016, *Monthly Notices of the Royal Astronomical Society*, **463**, 3653
- Kauffmann G., White S. D. M., Guiderdoni B., 1993, *MNRAS*, **264**, 201
- Kaushal N., Villaescusa-Navarro F., Giusarma E., Li Y., Hawry C., Reyes M., 2021, arXiv e-prints, [p. arXiv:2111.02441](https://arxiv.org/abs/2111.02441)
- Kingma D. P., Ba J., 2014, arXiv e-prints, [p. arXiv:1412.6980](https://arxiv.org/abs/1412.6980)
- Kitaura F.-S., Yepes G., Prada F., 2013, *Monthly Notices of the Royal Astronomical Society: Letters*, **439**, L21–L25
- Klypin A., Holtzman J., 1997, arXiv e-prints, [pp astro-ph/9712217](https://arxiv.org/abs/astro-ph/9712217)
- Kodi Ramanah D., Charnock T., Villaescusa-Navarro F., Wandelt B. D., 2020, *Monthly Notices of the Royal Astronomical Society*, **495**, 4227–4236
- Kravtsov A. V., Borgani S., 2012, *ARA&A*, **50**, 353
- Krizhevsky A., Sutskever I., Hinton G. E., 2017, *Commun. ACM*, **60**, 84–90
- Kwon D., Kim Y., Montúfar G., Yang I., 2021, arXiv e-prints, [p. arXiv:2110.14150](https://arxiv.org/abs/2110.14150)
- Lacey C., 2001, in Umemura M., Susa H., eds, Astronomical Society of the Pacific Conference Series Vol. 222, The Physics of Galaxy Formation. p. 273
- Le Cun Y., et al., 1989, *IEEE Communications Magazine*, **27**, 41
- LeNail A., 2019, *Journal of Open Source Software*, **4**, 747
- Li Y., Ni Y., Croft R. A. C., Di Matteo T., Bird S., Feng Y., 2021, *Proceedings of the National Academy of Sciences*, **118**, e2022038118
- Liguori M., Sefusatti E., Fergusson J. R., Shellard E. P. S., 2010, *Advances in Astronomy*, **2010**, 1–64
- Lin C.-A., Kilbinger M., 2015a, *Astronomy & Astrophysics*, **576**, A24
- Lin C.-A., Kilbinger M., 2015b, *Astronomy & Astrophysics*, **583**, A70
- Lin C.-A., Kilbinger M., Pires S., 2016, *Astronomy & Astrophysics*, **593**, A88
- Maas A., Hannun A., Ng A., 2013, in Proceedings of the International Conference on Machine Learning. Atlanta, Georgia

Mainini R., Romano A., 2014, *Journal of Cosmology and Astroparticle Physics*, 2014, 063–063

Marian L., Hilbert S., Smith R. E., Schneider P., Desjacques V., 2011, *ApJ*, **728**, L13

Martinet N., et al., 2018, *MNRAS*, **474**, 712

Mikkola S., Aarseth S. J., 1993, *Celestial Mechanics and Dynamical Astronomy*, **57**, 439

Mirza M., Osindero S., 2014, arXiv e-prints, p. [arXiv:1411.1784](https://arxiv.org/abs/1411.1784)

Monaco P., Theuns T., Taffoni G., Governato F., Quinn T., Stadel J., 2002, *The Astrophysical Journal*, **564**, 8

Monaco P., Sefusatti E., Borgani S., Crocce M., Fosalba P., Sheth R. K., Theuns T., 2013, *MNRAS*, **433**, 2389

Munshi D., Namikawa T., Kitching T. D., McEwen J. D., Takahashi R., Bouchet F. R., Taruya A., Bose B., 2020, *Monthly Notices of the Royal Astronomical Society*, **493**, 3985

Mustafa M., Bard D., Bhimji W., Lukić Z., Al-Rfou R., Kratochvil J. M., 2019, *Computational Astrophysics and Cosmology*, **6**, 1

Navarro J. F., Frenk C. S., White S. D. M., 1996, *ApJ*, **462**, 563

O’Shea B. W., Bryan G., Bordner J., Norman M. L., Abel T., Harkness R., Kritsuk A., 2004, arXiv e-prints, [pp astro-ph/0403044](https://arxiv.org/abs/ppastro-ph/0403044)

Papamakarios G., Nalisnick E., Jimenez Rezende D., Mohamed S., Lakshminarayanan B., 2019, arXiv e-prints, p. [arXiv:1912.02762](https://arxiv.org/abs/1912.02762)

Peebles P. J. E., 1993, *Principles of Physical Cosmology*. Princeton University Press

Percival W. J., 2005, *A&A*, **443**, 819

Percival W. J., Verde L., Peacock J. A., 2004, *Monthly Notices of the Royal Astronomical Society*, **347**, 645–653

Perraudin N., Srivastava A., Lucchi A., Kacprzak T., Hofmann T., Réfrégier A., 2019, *Computational Astrophysics and Cosmology*, **6**, 5

Pires S., Starck J.-L., Amara A., Réfrégier A., Teyssier, R. 2009, *A&A*, **505**, 969

Pires S., Leonard A., Starck J.-L., 2012, *Monthly Notices of the Royal Astronomical Society*, **423**, 983–992

Press W. H., Schechter P., 1974, *ApJ*, **187**, 425

Rizzo L. A., Villaescusa-Navarro F., Monaco P., Munari E., Borgani S., Castorina E., Sefusatti E., 2017, *Journal of Cosmology and Astroparticle Physics*, 2017, 008–008

Rodríguez A. C., Kacprzak T., Lucchi A., Amara A., Sgier R., Fluri J., Hofmann T., Réfrégier A., 2018, *Computational Astrophysics and Cosmology*, **5**

Ronneberger O., Fischer P., Brox T., 2015, arXiv e-prints, p. [arXiv:1505.04597](https://arxiv.org/abs/1505.04597)

Rouhiainen A., Giri U., Münchmeyer M., 2021, arXiv e-prints, p. [arXiv:2105.12024](https://arxiv.org/abs/2105.12024)

Sefusatti E., Crocce M., Pueblas S., Scoccimarro R., 2006, *Physical Review D*, **74**

Sefusatti E., Crocce M., Scoccimarro R., Couchman H. M. P., 2016, *Monthly Notices of the Royal Astronomical Society*, **460**, 3624–3636

Shan H., et al., 2018, *MNRAS*, **474**, 1116

Shao H., et al., 2022, *ApJ*, **927**, 85

Somerville R. S., Primack J. R., 1999, *Monthly Notices of the Royal Astronomical Society*, **310**, 1087

Springel V., 2005, *Monthly Notices of the Royal Astronomical Society*, **364**, 1105–1134

Springel V., et al., 2005, *Nature*, **435**, 629–636

de Swart J. G., Bertone G., van Dongen J., 2017, *Nature Astronomy*, **1**

Taruya A., Takada M., Hamana T., Kayo I., Futamase T., 2002, *The Astrophysical Journal*, **571**, 638–653

Tassev S., Zaldarriaga M., Eisenstein D. J., 2013, *Journal of Cosmology and Astroparticle Physics*, 2013, 036–036

Tassev S., Eisenstein D. J., Wandelt B. D., Zaldarriaga M., 2015, arXiv e-prints, p. [arXiv:1502.07751](https://arxiv.org/abs/1502.07751)

Taylor A., Joachimi B., 2014, *Monthly Notices of the Royal Astronomical Society*, **442**, 2728

Taylor A., Joachimi B., Kitching T., 2013, *Monthly Notices of the Royal Astronomical Society*, **432**, 1928–1946

Tormen G., 1997, *MNRAS*, **290**, 411

Tosone F., Neyrinck M. C., Granett B. R., Guzzo L., Vittorio N., 2020,

Table A1. Size of each layer’s output in the generator and the critic neural networks, detailed in Sect. 3.2 and Appendix A, for the high-resolution case. The low-resolution architecture is built analogously.

	Size	Comments
Generator	512×512×1	Input size; δ_{LN}
	256×256×64	
	128×128×128	First upsampling step
	64×64×256	
	32×32×512	
	64×64×512	
	128×128×256	
	256×256×128	
Critic	512×512×64	Linear activation; δ_{GEN}
	512×512×1	
	512×512×1	Input size; either δ_{SIM} or δ_{GEN}
	256×256×32	
	128×128×64	
	64×64×128	
	63×63×512	Flattening; input to dense layer
	62×62×1	
	3844	
	1	

MNRAS, **498**, 2663

Tosone F., Neyrinck M. C., Granett B. R., Guzzo L., Vittorio N., 2021, *MNRAS*, **505**, 2999

Trimble V., 1987, *Annual Review of Astronomy and Astrophysics*, **25**, 425

Villaescusa-Navarro F., et al., 2020, *The Astrophysical Journal Supplement Series*, **250**, 2

Villaescusa-Navarro F., et al., 2021, *The Astrophysical Journal*, **915**, 71

Watts P., Coles P., Melott A., 2003, *The Astrophysical Journal*, **589**, L61–L64

White S. D. M., Frenk C. S., 1991, *ApJ*, **379**, 52

White M., Tinker J. L., McBride C. K., 2013, *Monthly Notices of the Royal Astronomical Society*, **437**, 2594–2606

Xavier H. S., Abdalla F. B., Joachimi B., 2016, *Monthly Notices of the Royal Astronomical Society*, **459**, 3693–3710

Yamaguchi K., Sakamoto K., Akabane T., Fujimoto Y., 1990, in *The First International Conference on Spoken Language Processing, IC-SLP 1990*, Kobe, Japan, November 18–22, 1990. ISCA, http://www.isca-speech.org/archive/icslp_1990/i90_1077.html

Yiu T. W. H., Fluri J., Kacprzak T., 2021, arXiv e-prints, p. [arXiv:2112.12741](https://arxiv.org/abs/2112.12741)

Zhou J., et al., 2018, arXiv e-prints, p. [arXiv:1812.08434](https://arxiv.org/abs/1812.08434)

APPENDIX A: MODEL ARCHITECTURE

In its basic formulation, a layer in a convolutional neural network (CNN; see e.g. Fukushima 1980; Krizhevsky et al. 2017) is made of a certain number of square filters, each associated to learnable parameters, usually called weights. During training, each filter is convolved through each input data-point: this means that the dot product of the learnable weights and the input pixels is calculated, representing a single output for that particular filter. Repeating this operation while moving the filter across the input data creates an output map, which is then passed through an activation function to introduce non-linearities in the network. This operation is done for multiple filters, and each output map becomes the input to the following convolutional layer. Stacking convolutional layers allows one to extract progressively larger scales from the input data, and represents a more efficient implementation of a neural network with respect to standard dense layers when dealing with high-dimensional data like images (Le Cun et al. 1989; Goodfellow et al. 2016).

As anticipated, our model, depicted in Fig. 3, consists of two neural networks. The first neural network (the generator) contains four downsampling blocks, followed by four upsampling blocks. Each downsampling block first pads the input data assuming periodic boundary conditions, and then applies a convolution operation with 4×4 filters. There are 64 convolutional filters in the first place, and this number doubles for each block. Note that no pooling layers are present (Yamaguchi et al. 1990), and we are able to reduce the dimensionality of the extracted feature maps by shifting each filter by two pixels in both directions; in other words, we set a stride of 2. The compressed map is then symmetrically upsampled using the transposed convolution operation (Dumoulin & Visin 2016). At each block, each feature map is concatenated with the corresponding downsampled map by simply stacking them along the last spatial axis; this is done in order to better learn the representations at each level (Ronneberger et al. 2015). The activation function used after each downsampling layer is the rectified linear unit (ReLU, Glorot et al. 2011), while for the upsampling blocks we found the leaky ReLU (Maas et al. 2013) with $\alpha = 0.3$ to perform better. A final convolutional layer with linear activation function outputs the generated map δ_{GEN} . Note that all downsampling and upsampling blocks include batch normalisation (Ioffe & Szegedy 2015), which during training subtracts the batch mean and divides by the batch standard deviation, in order to make the training procedure more stable. The second neural network is done similarly, with three downsampling blocks followed by two convolutional layers with Leaky ReLU as the activation function, and a final dense layer with a single output and a linear activation function. Input and output shapes for each layer are reported in Table A1. We implement our neural networks in TENSORFLOW (Abadi et al. 2015), and will make the trained models available upon acceptance of this work.

This paper has been typeset from a \LaTeX file prepared by the author.